

Evaluation of the Bilinear Condensate of the Planar Thirring Model in the Strongly Coupled Region

Jude Worthy

*Department of Physics, College of Science, Swansea University
Swansea SA2 8PP, United Kingdom
jagworthy887140@swansea.ac.uk*

Simon Hands

*Department of Mathematical Sciences, University of Liverpool
Liverpool, L69 3BX, United Kingdom
simon.hands@liverpool.ac.uk*

The planar Thirring model is thought to have a strongly coupled critical point for a single flavour of fermion. We look at the calculation of the bilinear condensate in this critical region, and its characterisation via an equation of state. Since the computation is numerically challenging we investigate improved Dirac operators. We present findings on different methods of calculation using a rational hybrid Monte Carlo scheme, and calculations of the bilinear condensate, an equation of state, and the associated critical exponents. Overlap and domain wall Dirac operators, and variants therein are considered.

Keywords: Thirring Model; Overlap Operator; Domain Wall Operator; Condensate; Criticality; Planar Fermions

1. Introduction

The Euclidean continuum formulation of the Thirring model² for a single fermion field in $2 + 1d$ is given by:¹

$$S[\psi, \bar{\psi}] = \int d^3x \bar{\psi}(\gamma_\mu \partial_\mu + m)\psi + \frac{g^2}{2}(\bar{\psi}\gamma_\mu\psi)^2 \quad (1)$$

The self interacting term of the conserved current $\bar{\psi}\gamma_\mu\psi$ may be reformulated using an auxiliary vector field A_μ to yield a physically equivalent action $S[\psi, \bar{\psi}, A] = S_F[\psi, \bar{\psi}, A] + S_G[A]$, where the fermionic action S_F takes the usual gauge invariant form while the auxiliary action $S_G[A]$ is *not* gauge invariant:

$$S_F[\psi, \bar{\psi}, A] = \int d^3x \bar{\psi}(\gamma_\mu(\partial_\mu + iA_\mu) + m)\psi \quad (2)$$

$$S_G[A] = \frac{1}{2g^2} \int d^3x A_\mu^2 \quad (3)$$

In a planar $(2+1d)$ formulation the Dirac field ψ may be irreducible (2-component), wherein the gamma matrices are given by the Pauli matrices, but the Lagrangian

(1,2) is then not parity invariant with the inclusion of a mass term $m \neq 0$. Instead we choose a reducible 4-component field, for which $m\bar{\psi}\psi$ is parity invariant. In particular there are two independent parity transforms, a γ_3 -transform, and a γ_5 -transform, which under a reflection of coordinates $x_\mu \rightarrow -x_\mu$ ($\mu = 0, 1, 2$) transform with, for $\gamma_j \in \{\gamma_3, \gamma_5\}$:

$$\begin{aligned} \psi &\rightarrow i\gamma_j\psi ; \quad \bar{\psi} \rightarrow -i\bar{\psi}\gamma_j \\ A &\rightarrow -A \end{aligned} \tag{4}$$

The 4-component field also admits a $U(2)$ global symmetry described by eqns. (5), explicitly breaking to a $U(1) \otimes U(1)$ with a non-zero mass; eqns. 5c, 5d do not hold for $m \neq 0$. These rotations are analogous to chiral symmetry in 3+1d formulations, and in the presence of interactions may also be spontaneously broken at and beyond a critical point. With fixed coordinates

$$\psi \rightarrow e^{i\alpha}\psi ; \quad \bar{\psi} \rightarrow \bar{\psi}e^{-i\alpha} \tag{5a}$$

$$\psi \rightarrow e^{i\alpha\gamma_3\gamma_5}\psi ; \quad \bar{\psi} \rightarrow \bar{\psi}e^{-i\alpha\gamma_3\gamma_5} \tag{5b}$$

$$\psi \rightarrow e^{i\alpha\gamma_3}\psi ; \quad \bar{\psi} \rightarrow \bar{\psi}e^{i\alpha\gamma_3} \tag{5c}$$

$$\psi \rightarrow e^{i\alpha\gamma_5}\psi ; \quad \bar{\psi} \rightarrow \bar{\psi}e^{i\alpha\gamma_5} \tag{5d}$$

We may separate the Dirac spinors into ‘‘left handed’’ (+) and ‘‘right handed’’ (–) components. In 3+1d this distinction is uniquely determined by the chirality operator γ_5 , with projectors $P_\pm^5 = (1 \pm \gamma_5)/2$ isolating each handedness. In 2+1d the distinction is not unique and we may also choose γ_3 , with $P_\pm^3 = (1 \pm \gamma_3)/2$. A γ_3 -parity transform swaps a P^3 -left spinor into a P^3 -right spinor and vice versa, and similarly for the γ_5 -parity transform.

We also have a continuous family of $U(2)$ -equivalent mass terms,³ from which we extract and label $m\bar{\psi}\psi$, $im\bar{\psi}\gamma_3\psi$ as the standard and twisted mass formulations respectively.

On a space-time lattice with spacing a we encounter the Nielsen-Ninomiya no-go theorem, rendering $U(2)$ symmetry incompatible with the locality of the Dirac operator, and no lattice doublers. A work-around is given by the Ginsparg-Wilson relations,⁴ in which the $U(2)$ transformations are adjusted according to:³

$$\begin{aligned} \psi &\rightarrow e^{i\alpha\gamma_3(1-\frac{aD}{2})}\psi ; \quad \bar{\psi} \rightarrow \bar{\psi}e^{i\alpha\gamma_3(1-\frac{aD}{2})} \\ \psi &\rightarrow e^{i\alpha\gamma_5(1-\frac{aD}{2})}\psi ; \quad \bar{\psi} \rightarrow \bar{\psi}e^{i\alpha\gamma_5(1-\frac{aD}{2})}, \end{aligned} \tag{6}$$

where the Dirac operator D satisfies

$$\{\gamma_3, D\} = 2aD\gamma_3D; \quad \{\gamma_5, D\} = 2aD\gamma_5D; \quad [\gamma_3\gamma_5, D] = 0. \tag{7}$$

For any such D , in the continuum limit $a \rightarrow 0$ we see that $U(2) \rightarrow U(1) \otimes U(1)$ is recovered. This is contingent on the locality of the operator, which ensures $aD \rightarrow 0$.

The continuum limit corresponds to a critical point in the phase diagram of the lattice Thirring model. Besides explicit symmetry breaking the Thirring model has been demonstrated to spontaneously break $U(2) \rightarrow U(1) \otimes U(1)$, analogously to

chiral symmetry breaking, with the bilinear condensate $\langle \bar{\psi}\psi \rangle$ as the order parameter. Around this critical point we construct an empirical equation of state,⁵ defining the behaviour of the order parameter in the critical region.

$$m = A(\beta - \beta_c) \langle \bar{\psi}\psi \rangle^{\delta-1/\beta_m} + B \langle \bar{\psi}\psi \rangle^\delta. \quad (8)$$

The existence and calculated properties of the critical point have been found to depend on the type of lattice model used. The critical flavour number is the maximum number of fermion flavours which allow a critical point. Domain wall techniques¹ find this critical flavour number to be $N_f = 1$, distinct from both staggered⁶ ($N_f > 1$) and SLAC⁷ ($N_f < 1$) lattice fermion formulations. The values of the associated critical exponents β_m, δ differ as well.

We continue to choose the overlap Dirac operator^{8,9}

$$D_{OL} = \frac{1 + im\gamma_3}{2} + \gamma_3 \text{sgn}(H) \frac{1 - im\gamma_3}{2} \quad (9)$$

as most suitable for our discretisation of the fermionic terms, since it obeys the Ginsparg-Wilson relations,⁴ enabling the recovery of the desired global U(2) symmetry in the continuum limit. Choices in the implementation of the overlap operator include the kernel of the sign function H , the approximation to the sign function, a further regularization parameter M , and the form of the bare mass term,^{3,10} all of which we expect to be physically equivalent in the U(2)-symmetric continuum limit. After an approximation to the sign function is chosen the operator is often referred to as a truncated overlap operator. The domain wall operator D_{DW} , specified more fully in Section 3.3 below, is expressed with an additional non-physical dimension x_3 separating two open boundaries or “domain walls” by an extent L_s , may be chosen to be exactly related to a truncated overlap operator¹⁰⁻¹² and hence an overlap operator in the limit $L_s \rightarrow \infty$. In such cases the regularization parameter M is equivalently the domain wall height. Consequently, formulations may be chosen so that numerically identical results are found with either D_{OL} or D_{DW} , as shown in Section 4.3. The domain wall formulation is more convenient for the generation and evolution of the auxiliary fields via the Rational Hybrid Monte Carlo (RHMC) method. When the Wilson kernel ($H = \gamma_3 D_W$) is chosen it is preferable to use the overlap operator given by (9) in the measurement calculations, where $D_W[A]$ is the usual Wilson Dirac operator specified in (14) below. When the Shamir kernel ($H = \gamma_3 D_W (2 + D_W)^{-1}$) is chosen the domain wall formulation is generally preferable. Significant cost benefits in condensate calculations have been demonstrated with the twisted mass form³ as specified in (9).

Using domain wall Dirac operators D_{DW} a critical point has been found with a single fermion flavour but not with two or more, and hence we use RHMC¹³ for the generation of the auxiliary fields - the single fermion in the effective action is given by $(D_{DW}^\dagger D_{DW})^{-1/2}$ for which we use a rational approximation.

The lattice Thirring model for a single fermion is given by action^a

$$S_{\text{Th}} = \psi^\dagger (D_{DW}[U_\mu]^\dagger D_{DW}[U_\mu])^{1/2} \psi + \beta A_\mu^2 \quad (10)$$

where the coupling parameter $\beta = \frac{a}{g^2}$ is adimensional. The link field U in the operator $D_{DW}[U]$ is generated with non-compact relation $U_\mu = 1 + iaA_\mu$ rather than the compact relation $U_\mu = e^{iaA_\mu}$ used for lattice QED. Periodic boundary conditions are applied in the two spatial dimensions and require no adjustment, but an anti-periodic boundary condition in the temporal dimension is specified for the time components of the link field on the time dimension boundary, so that $U_0(T, x, y) = -U_0(1, x, y)$ for all x, y . The lattice spacing a is set to 1 in all of the following.

2. Condensate Measurements

The bilinear condensate order parameter is defined by

$$\frac{\partial \ln \mathcal{Z}}{\partial m} = \left\langle \text{Tr} \left[\frac{\partial \ln D(m)}{\partial m} \right] \right\rangle = \left\langle \text{Tr} \left[D^{-1} \frac{\partial D}{\partial m} \right] \right\rangle, \quad (11)$$

where the partition function is defined by the functional integral $\mathcal{Z} = \int \mathcal{D}\psi \mathcal{D}\bar{\psi} \mathcal{D}A e^{-S[\psi, \bar{\psi}, A]}$. We consider Dirac operators which separate out the mass component $D[U] = D^0[U] + mD^M[U]$. We estimate the bilinear condensate over N instances with distinct auxiliary fields U_i , using Monte Carlo integration

$$\langle \bar{\psi}\psi \rangle = \frac{1}{N} \sum_{i=1}^N \frac{1}{V} \text{Tr}[D^M[U_i]D[U_i]^{-1}] \quad (12)$$

where V is the number of vertices in the lattice. We use the RHMC method^{13,14} outlined further below, for the generation of auxiliary fields A_i , and consequently U_i , for each instance. We choose overlap Dirac operators (see (18) below), so that $D_{OL}^0[U] = \frac{1}{2} + \frac{1}{2}V[U]$ and we distinguish two mass variants, the standard $D_{OL}^{M1}[U] = \frac{1}{2} - \frac{1}{2}V[U]$, and twisted $D_{OL}^{M3}[U] = \frac{i\gamma_3}{2} - V[U]\frac{i\gamma_3}{2}$, in which $V[U] = \gamma_3 \text{sgn}[H[U]]$. More details are given below, but regardless of the choice of kernel $H[U]$ we have the condensate instances

$$\begin{aligned} \hat{O}_{OL}^1 &= \frac{1}{V} \text{Tr} \left[\frac{1}{1-m} ((D_{OL}^1)^{-1} - 1) \right]; \\ \hat{O}_{OL}^3 &= \frac{1}{V} \text{Tr} \left[\frac{-1}{i\gamma_3 + m} ((D_{OL}^3)^{-1} - 1) \right] \end{aligned} \quad (13)$$

corresponding to $D_{OL}^1 = D_{OL}^0 + mD_{OL}^{M1}$ and $D_{OL}^3 = D_{OL}^0 + mD_{OL}^{M3}$. A noisy estimator may be used to calculate the trace, according to algorithm 1, with $N_N = 10$ used in this work.

^aNote that the power $1/2 \rightarrow -1/2$ when moving from the Grassmann field ψ in the action, to the complex-valued pseudofermion ψ in the effective action.

Algorithm 1 Noisy estimator for the trace of the inverse of a complex matrix M

```

1: function CALCULATENOISYESTIMATOR( $M$ )
2:   Set  $s = 0$ 
3:   for  $n = 1, N_N$  do %  $N_N$  is the number of noisy estimators per instance
4:      $\eta = \mathcal{CN}(0, 1)$  % vector of complex Gaussian random numbers
5:      $\xi = M^{-1}\eta$ 
6:      $s = s + \eta^\dagger \xi$ 
7:   return  $s/N_N$ 

```

3. Dirac Operators

We want measurements calculated with the overlap operator. Domain wall operators may be formally equivalent to overlap operators when the Pauli-Villars terms to compensate for the influence of unphysical bulk fields with $1 < x_3 < L_s$ are included (see below), and it is often computationally advantageous to use the domain wall formulation. Variants of D_{OL} , and similarly the equivalent D_{DW} , include the choice of mass term - standard or twisted, the choice of kernel - Shamir or Wilson, and the choice of kernel approximation method - hyperbolic tangent (HT) or Zolotarev (Z). Whether to use D_{DW} or D_{OL} formulation is context dependent, although table 1 provides a guide in which we distinguish between the valence fermion Dirac operator - that used in the Monte Carlo integration of eqn. (12) - and the sea fermion operator - that used in the effective action (35) below, used in the hybrid Monte Carlo algorithms for the generation of the auxiliary fields. All of these

Table 1. Guide to choice of overlap formulation

	Valence	Sea
Strongly coupled	Twisted Wilson Zolo $\Leftrightarrow D_{OL}$	Twisted Wilson HT $\Leftrightarrow D_{DW}$
Weakly coupled	Twisted Shamir HT $\Leftrightarrow D_{DW}$	Twisted Shamir HT $\Leftrightarrow D_{DW}$

variants are constructed from the Wilson Dirac operator $D_W[U]$. Derivatives of the Dirac operators are required in hybrid Monte Carlo algorithms, and may similarly be constructed via the derivatives of D_W . The operators and algorithms for their application are given below.

3.1. Wilson Dirac Operator

The continuum Euclidean Dirac operator is given by $D_E \equiv \gamma_\mu(\partial_\mu + iA_\mu) + m$, and its conjugate is $D_E^\dagger \equiv -\gamma_\mu(\partial_\mu + iA_\mu) + m$. We choose complex link fields given by $U_\mu = 1 + iA_\mu$ rather than the usual compact $U_\mu = e^{iA_\mu}$ form, eliminating six-point and higher order interaction coupling terms in the discretisation of (1) once the auxiliary fields are integrated over. The lattice Wilson Dirac operator D_W applied

to lattice node n is then given by

$$(D_W\psi)(n) = \frac{1}{2} \sum_{\mu=0,1,2} [\gamma_\mu(U_\mu(n)\psi(n+\hat{\mu}) - U_\mu(n-\hat{\mu})^\dagger\psi(n-\hat{\mu})) - (U_\mu(n)\psi(n+\hat{\mu}) - 2\psi(n) + U_\mu(n-\hat{\mu})^\dagger\psi(n-\hat{\mu}))] + m\psi(n) \quad (14)$$

The first line of (14) gives the Dirac term, corresponding to the massless part of the continuum operator, and the second line of (14) is the Wilson term, introduced to remedy the so-called lattice doubling problem.²¹ The conjugate operator D_W^\dagger changes the sign of the Dirac term, but not the Wilson term. The derivative operator is given by

$$\left(\frac{\partial D_W}{\partial A_{x,\mu}}\psi\right)(n) = \begin{cases} \frac{1}{2}\gamma_\mu\psi(x+\hat{\mu})i - \frac{1}{2}\psi(x+\hat{\mu})i, & n = x \\ \frac{1}{2}\gamma_\mu\psi(x)i + \frac{1}{2}\psi(x)i, & n = x + \hat{\mu} \\ 0 & \text{otherwise} \end{cases} \quad (15)$$

and hence for arbitrary complex spinor fields η, ν

$$\eta^\dagger \frac{\partial D_W}{\partial A_{x,\mu}} \nu = \frac{1}{2}\eta(x)^\dagger \gamma_\mu i \nu(x+\hat{\mu}) - \frac{1}{2}\eta(x)^\dagger i \nu(x+\hat{\mu}) + \frac{1}{2}\eta(x+\hat{\mu})^\dagger i \gamma_\mu \nu(x) + \frac{1}{2}\eta(x+\hat{\mu})^\dagger i \nu(x) \quad (16)$$

Again, the conjugate $\frac{\partial D_W^\dagger}{\partial A_{x,\mu}}$ changes the sign of the Dirac term. We can then calculate the Wilson derivative matrix, F_{D_W} , and conjugate $F_{D_W}^\dagger$ used in the RHMC algorithm as set out in algorithm 2, where

$$F_{D_W} = \eta^\dagger \frac{\partial D_W}{\partial A} \nu \quad ; \quad F_{D_W}^\dagger = \eta^\dagger \frac{\partial D_W^\dagger}{\partial A} \nu \quad (17)$$

Algorithm 2 Wilson Dirac Derivatives

```

1: function WILSONDERIVS( $\eta, \nu, \text{DAG}$ ) % eqn 17 via eqn 16
2:   for all  $x, \mu$  do
3:     if  $\text{DAG}=\text{FALSE}$  then
4:        $F((x, \mu) = \eta(x)^\dagger \gamma_\mu i \nu(x+\hat{\mu})/2 + \eta(x+\hat{\mu})^\dagger \gamma_\mu i \nu(x)/2$ 
5:          $- \eta(x)^\dagger i \nu(x+\hat{\mu})/2 + \eta(x+\hat{\mu})^\dagger \gamma_\mu i \nu(x)/2$ 
6:     else if  $\text{DAG}=\text{TRUE}$  then
7:        $F((x, \mu) = -\eta(x)^\dagger \gamma_\mu i \nu(x+\hat{\mu})/2 + \eta(x+\hat{\mu})^\dagger \gamma_\mu i \nu(x)/2$ 
8:          $- \eta(x)^\dagger i \nu(x+\hat{\mu})/2 + \eta(x+\hat{\mu})^\dagger \gamma_\mu i \nu(x)/2$ 
9:   return  $F$ 

```

3.2. Overlap Dirac Operator

The overlap Dirac operator^{8,9} is usually given by $D_{OL}^1 = \frac{1+m}{2} + \frac{1-m}{2}V$. The twisted mass formulation enabled by the planar dimensionality may be expressed with the following in which $V = \gamma_3 \text{sgn}(H)$ ¹¹ (Cf. eqn. (9)).

$$\begin{aligned} D_{OL}^3 &= \frac{1 + im\gamma_3}{2} + V \frac{1 - im\gamma_3}{2} \\ D_{OL}^{3\dagger} &= \frac{1 - im\gamma_3}{2} + \frac{1 + im\gamma_3}{2} V^\dagger \end{aligned} \quad (18)$$

$H \equiv \gamma_3 D_W$ specifies the Wilson kernel. We are also interested the formulation with Shamir kernel for which $H = \frac{\gamma_3 D_W}{2+D_W}$ and which corresponds to the usual domain wall formulation due to Shamir.²³ Noting $\text{sgn}(H) \equiv H(H^2)^{-1/2}$, and $\gamma_3 D_W \gamma_3 = D_W^\dagger$, for the Wilson kernel we have

$$\begin{aligned} V &= D_W (D_W^\dagger D_W)^{-1/2} \\ V^\dagger &= D_W^\dagger (D_W^\dagger D_W)^{-1/2} \end{aligned} \quad (19)$$

Note that m is the bare mass; the Wilson Dirac operator (14) in the kernel H has mass term $M\bar{\psi}\psi$ with a regularisation parameter $-2 < M < 0$ in place of the usual mass term $m\bar{\psi}\psi$. $M = -1$ in this work. The inverse square root, exponent $p = -1/2$, must be approximated, and we do so with a partial fraction formulation of a corresponding rational function. This is then sometimes referred to as a truncated overlap operator. We will also want to evaluate other operators similarly with powers other than $p = -1/2$, notably $p = 1/4$. For arbitrary operators D and different powers p , the partial fraction formulation of a rational function approximation of $(D^\dagger D)^p$ is given by

$$(D^\dagger D)^p = \alpha_{0,p} + \sum_i \frac{\alpha_{i,p}}{D^\dagger D + \beta_{i,p}} \quad (20)$$

The denominators may be evaluated, for example, successively with a conjugate gradient algorithm, or simultaneously with a multishift conjugate gradient algorithm.¹⁸ When the Shamir kernel is used this is slow to calculate and it is computationally faster to calculate measurements using a domain wall formulation instead; this formulation does provides a cross check of any code however.

The choice of coefficients α, β is significant. From the hyperbolic tangent approximation to the sign function, $\text{sgn}(x) \approx \tanh(n \tanh^{-1} x)$, we have the partial fraction expression for even n :¹⁰

$$\text{sgn}(x) \approx \frac{2x}{n} \sum_{j=0}^{n/2-1} \frac{1 + (\tan \frac{(j+1/2)\pi}{n})^2}{x^2 + (\tan \frac{(j+1/2)\pi}{n})^2} \quad (21)$$

The inverse root power may be taken from $x^{-1/2} = \text{sgn}(x^{1/2})/x^{1/2}$. Alternatively we may use an optimal Zolotarev approximation²⁵ to the sign function^b. The coefficients depend on the specified range of the approximation. That is, we have the

^bThe Zolotarev approximation to the inverse root power is, of course, similarly related

Zolotarev functions $\mathcal{Z}_n^{x_L, x_R}(x) \approx \text{sgn}(x)$ in the range $x \in [x_L, x_R]$, and with accuracy increasing with order n . This range must encompass the spectral range of the kernel H . These can be calculated analytically,^{27,28} or more generally using the Remez algorithm, which also allows the calculation of coefficients for other powers. There is freely available software to calculate the coefficients via the iterative Remez algorithm.²² There should be *a priori* knowledge of the spectral range if one is to avoid recalculating the coefficients for every distinct auxiliary field.

3.3. Domain Wall Operators

The domain wall operators have an extra dimension of discrete extent L_s , and we label an extended fermion field Ψ , denoting slices indexed along the extra dimension $j = 1, \dots, L_s$ with ψ_j . Application of the domain wall operator may be carried out by application of the Wilson Dirac operator on different slices according to the following.^{11,19,23} We will specify both Shamir and Wilson kernel variants, each with a standard and twisted mass formulation.

3.3.1. Shamir Kernel Domain Wall Dirac Operator

We consider two forms: $D_{SDW}^3 = D_{SDW}^0 + mD_{SDW}^{M3}$, and $D_{SDW}^1 = D_{SDW}^0 + mD_{SDW}^{M1}$. In either case the massless expression $\Psi' = D_{SDW}^0 \Psi$ has components

$$\psi'_j = \begin{cases} (D_W + I)\psi_j - P_- \psi_{j+1} & j = 1 \\ -P_+ \psi_{j-1} + (D_W + I)\psi_j - P_- \psi_{j+1} & 1 < j < L_s \\ -P_+ \psi_{j-1} + (D_W + I)\psi_j & j = L_s \end{cases} \quad (22)$$

with projectors $P_{\pm} \equiv P_{\pm}^3$ defined earlier. The conjugate operator, with $\bar{\Psi}' = (D_{SDW}^0)^\dagger \Psi$ is given by

$$\bar{\psi}'_j = \begin{cases} (D_W^\dagger + I)\psi_j - P_+ \psi_{j+1} & j = 1 \\ -P_- \psi_{j-1} + (D_W + I)\psi_j - P_+ \psi_{j+1} & 1 < j < L_s \\ -P_- \psi_{j-1} + (D_W + I)\psi_j & j = L_s \end{cases} \quad (23)$$

Standard (mD_{SDW}^{M1}) mass components and their conjugate counterparts contribute

$$\begin{aligned} \psi'_1 &= mP^+ \psi_{L_s} & \bar{\psi}'_1 &= mP^- \psi_{L_s} \\ \psi'_{L_s} &= mP^- \psi_1 & \bar{\psi}'_{L_s} &= mP^+ \psi_1 \end{aligned} \quad (24)$$

The twisted (mD_{SDW}^{M3}) mass components contribute^c

$$\begin{aligned} \psi'_1 &= -imP^+ \gamma_3 \psi_{L_s} & \bar{\psi}'_1 &= im\gamma_3 P^- \psi_{L_s} \\ \psi'_{L_s} &= -imP^- \gamma_3 \psi_1 & \bar{\psi}'_{L_s} &= im\gamma_3 P^+ \psi_1 \end{aligned} \quad (25)$$

The derivatives $\partial D_{SDW} / \partial A$ are described along with the Wilson kernel in 3.3.2 below, since they are identical to the diagonal components of that scheme.

^cNote $P^+ \gamma_3 = \gamma_3 P^+ = P^+$ and $P^- \gamma_3 = \gamma_3 P^- = -P^-$

3.3.2. Wilson Kernel Domain Wall Dirac Operator

We again distinguish two forms via the standard and twisted mass terms, $D_{WDW}^3 = D_{WDW}^0 + mD_{WDW}^{M3}$, and $D_{WDW}^1 = D_{WDW}^0 + mD_{WDW}^{M1}$. We now further denote $D_j^+ = \omega_j D_W + I$, $D_j^- = \omega_j D_W - I$. Setting the coefficients $\omega_j = 1$ corresponds to the hyperbolic tangent approximation of the sign function. To obtain the Zolotarev approximation we set $\omega_j = 1/u_j$ where u_j are the roots of $\mathcal{Z}_n^{xL, xR}(x) - 1 = 0$. Code to calculate these roots and the Zolotarev coefficients directly is also freely available.²⁹ For the massless component we have

$$\psi'_j = \begin{cases} D_j^+ \psi_j + D_j^- P_- \psi_{j+1} & j = 1 \\ D_j^- P_+ \psi_{j-1} + D_j^+ \psi_j + D_j^- P_- \psi_{j+1} & 1 < j < L_s \\ D_j^- P_+ \psi_{j-1} + D_j^+ \psi_j & j = L_s \end{cases} \quad (26)$$

The conjugate operator, with $\bar{\psi}'_j \equiv ((D_{WDW}^0)^\dagger) \Psi(j)$, $D_j^{\dagger+} = \omega_j D_W^\dagger + I$, $D_j^{\dagger-} = \omega_j D_W^\dagger - I$, is

$$\bar{\psi}'_j = \begin{cases} D_j^{\dagger+} \psi_j + P_+ D_{j+1}^{\dagger-} \psi_{j+1} & j = 1 \\ P_- D_{j-1}^{\dagger-} \psi_{j-1} + D_j^{\dagger+} \psi_j + P_+ D_{j+1}^{\dagger-} \psi_{j+1} & 1 < j < L_s \\ P_- D_{j-1}^{\dagger-} \psi_{j-1} + D_j^{\dagger+} \psi_j & j = L_s \end{cases} \quad (27)$$

Standard (mD_{WDW}^{M1}) mass components and their conjugate counterparts contribute

$$\begin{aligned} \psi'_1 &= -mD_1^- P^+ \psi_{L_s} & \bar{\psi}'_1 &= -mP^- D_{L_s}^{\dagger-} \psi_{L_s} \\ \psi'_{L_s} &= -mD_{L_s}^- P^- \psi_1 & \bar{\psi}'_{L_s} &= -mP^+ D_1^{\dagger-} \psi_1 \end{aligned} \quad (28)$$

The twisted (D_{WDW}^{M3}) mass components contribute

$$\begin{aligned} \psi'_1 &= -imD_1^- P^+ \gamma_3 \psi_{L_s} & \bar{\psi}'_1 &= im\gamma_3 P^- D_{L_s}^{\dagger-} \psi_{L_s} \\ \psi'_{L_s} &= -imD_{L_s}^- P^- \gamma_3 \psi_1 & \bar{\psi}'_{L_s} &= im\gamma_3 P^+ D_1^{\dagger-} \psi_1 \end{aligned} \quad (29)$$

The derivative term $\frac{\partial D_{DW}}{\partial A_{x,d}} \Psi$ has component slices ψ'_j for the massless parts given by

$$\psi'_j = \left(\frac{\partial D_{DW}^0}{\partial A_{x,d}} \Psi \right) (j) = \begin{cases} \omega_j \frac{\partial D_W}{\partial A_{x,\nu}} \psi_j + \omega_j \frac{\partial D_W}{\partial A_{x,\nu}} P_- \psi_{j+1} & j = 1 \\ \omega_j \frac{\partial D_W}{\partial A_{x,\nu}} P_+ \psi_{j-1} + \omega_j \frac{\partial D_W}{\partial A_{x,\nu}} \psi_j + \omega_j \frac{\partial D_W}{\partial A_{x,\nu}} P_- \psi_{j+1} & 1 < j < L_s \\ \omega_j \frac{\partial D_W}{\partial A_{x,\nu}} P_+ \psi_{j-1} + \omega_j \frac{\partial D_W}{\partial A_{x,\nu}} \psi_j & j = L_s \end{cases} \quad (30)$$

$$\bar{\psi}'_j = \left(\frac{\partial D_{DW}^{0\dagger}}{\partial A_{x,d}} \Psi \right) (j) = \begin{cases} \omega_j \frac{\partial D_W^\dagger}{\partial A_{x,d}} \psi_j + P_+ \omega_{j+1} \frac{\partial D_W^\dagger}{\partial A_{x,d}} \psi_{j+1} & j = 1 \\ P_- \omega_{j-1} \frac{\partial D_W^\dagger}{\partial A_{x,d}} \psi_{j-1} + \omega_j \frac{\partial D_W^\dagger}{\partial A_{x,d}} \psi_j + P_+ \omega_{j+1} \frac{\partial D_W^\dagger}{\partial A_{x,d}} \psi_{j+1} & 1 < j < L_s \\ P_- \omega_{j-1} \frac{\partial D_W^\dagger}{\partial A_{x,d}} \psi_{j-1} + \omega_j \frac{\partial D_W^\dagger}{\partial A_{x,d}} \psi_j & j = L_s \end{cases} \quad (31)$$

and for the mass parts by

$$\psi'_j = \frac{\partial D_{DW}^M}{\partial A_{x,d}} \psi = \begin{cases} -\omega_1 \frac{\partial D_W}{\partial A_{x,d}} P^+ c \psi_{L_s} & j = 1 \\ -\omega_{L_s} \frac{\partial D_W}{\partial A_{x,d}} P^- c \psi_1 & j = L_s \\ 0 & \text{otherwise} \end{cases} \quad (32)$$

$$\bar{\psi}'_j = \frac{\partial D_{DW}^{M\dagger}}{\partial A_{x,d}} \psi = \begin{cases} -\omega_{L_s} c^\dagger P^- \frac{\partial D_W^\dagger}{\partial A_{x,d}} \psi_{L_s} & j = 1 \\ -\omega_1 c^\dagger P^+ \frac{\partial D_W^\dagger}{\partial A_{x,d}} \psi_1 & j = L_s \\ 0 & \text{otherwise} \end{cases} \quad (33)$$

For the standard mass term $c = c^\dagger = 1$, and for the twisted mass term $c = i\gamma_3$, $c^\dagger = -i\gamma^3$.

Algorithms 3 and 4 put together the domain wall derivative matrix, $F_{D_{DW}} = \boldsymbol{\eta} \frac{\partial D_{DW}}{\partial A} \boldsymbol{\nu}$, and conjugate $F_{D_{DW}}^\dagger = \boldsymbol{\eta} \frac{\partial D_{DW}^\dagger}{\partial A} \boldsymbol{\nu}$.

Algorithm 3 DomainWallDerivs. Returns array $F_{D_{DW}} = \boldsymbol{\eta} \frac{\partial D_{DW}}{\partial A} \boldsymbol{\nu}$ or $F_{D_{DW}}^\dagger = \boldsymbol{\eta} \frac{\partial D_{DW}^\dagger}{\partial A} \boldsymbol{\nu}$ via eqns. 30,31.

```

1: function DOMWALLDERIVS( $\boldsymbol{\eta}, \boldsymbol{\nu}, MTYPE, DAG$ )
2:    $F = 0$ 
3:   % diagonal components
4:   for  $j = 1, \dots, L_s$  do
5:      $F = F + \text{WILSONDERIVS}(\boldsymbol{\eta}(j), \boldsymbol{\nu}(j), DAG)$ 
6:     % if using Shamir kernel, return here
7:
8:     % upper and lower diagonal components
9:     for  $j = 1, \dots, L_s - 1$  do
10:       $F = F + \text{WILSONDERIVS}(\boldsymbol{\eta}(j), \boldsymbol{\nu}(j+1), DAG)$ 
11:       $F = F + \text{WILSONDERIVS}(\boldsymbol{\eta}(j+1), \boldsymbol{\nu}(j), DAG)$ 
12:     % Mass terms
13:      $F = F + \text{DOMWALLMASSDERIVS}(\boldsymbol{\eta}, \boldsymbol{\nu}, MTYPE, DAG)$ 
14:   return  $F$ 

```

Algorithm 4 DomainWallMassDerivs. Returns the mass components of $F_{D_{DW}}$ via eqns. 32, 33.

```

1: function DOMWALLMASSDERIVS( $\eta, \nu, \text{MTYPE}, \text{DAG}$ )
2:   % mass components
3:   if (MTYPE.eq.STANDARD).AND.(DAG.eq.FALSE) then
4:      $l_1 = \eta(1)$  ;  $r_1 = -\omega_1 P^+ \nu(L_s)$ 
5:      $l_2 = \eta(L_s)$  ;  $r_2 = -\omega_{L_s} P^- \nu(1)$ 
6:   else if (MTYPE.eq.STANDARD).AND.(DAG.eq.TRUE) then
7:      $l_1 = -\omega_{L_s} P^- \eta(1)$  ;  $r_1 = \nu(L_s)$ 
8:      $l_2 = -\omega_{L_s} P^+ \eta(L_s)$  ;  $r_2 = \nu(1)$ 
9:   else if (MTYPE.eq.TWISTED).AND.(DAG.eq.FALSE) then
10:     $l_1 = \eta(1)$  ;  $r_1 = -i\omega_1 P^+ \gamma_3 \nu(L_s)$ 
11:     $l_2 = \eta(L_s)$  ;  $r_2 = -i\omega_{L_s} P^- \gamma_3 \nu(1)$ 
12:  else if (MTYPE.eq.TWISTED).AND.(DAG.eq.TRUE) then
13:     $l_1 = -i\omega_{L_s} \gamma_3 P^- \eta(1)$  ;  $r_1 = \nu(L_s)$ 
14:     $l_2 = -i\omega_{L_s} \gamma_3 P^+ \eta(L_s)$  ;  $r_2 = \nu(1)$ 
15:  return WILSONDERIVS( $l_1, r_1$ ) + WILSONDERIVS( $l_2, r_2$ )

```

4. Generation of Auxiliary Fields - Hybrid Monte Carlo

We want to generate independent random auxiliary fields A with probability distribution $P[A] \propto e^{-S[A]}$, for our Thirring action $S[A]$, eqn. 10. We generate a sequence A^0, \dots, A^N using a hybrid Monte Carlo method. For N large enough, A_N will take the specified distribution $\propto e^{-S[A]}$, regardless of the choice of A_0 . Each step of the sequence comprises a hamiltonian dynamics component, which generates a proposed field A' , followed by a Monte Carlo acceptance step, in which the proposed field is either accepted or rejected as the next field in the sequence, as set out in algorithm 5.

Algorithm 5 Hybrid Monte Carlo generation of a randomly distributed auxiliary field. Step 1: Generate a proposed auxiliary field. Step 2: Monte Carlo acceptance

```

1: function GENERATENEXTAUX( $A^0$ )
2:   for s=1 to S do
3:     [ $A', P^{s-1}, P', \phi$ ] = GENPROPAUX( $A^{s-1}$ )
4:      $A^s$  = MCACCEPTANCE( $A^{s-1}, A', P^{s-1}, P', \phi$ )
5:   return  $A^S$ 

```

4.1. Hamiltonian Dynamics

The proposed field A' is found by time marching the artificially created hamiltonian system $H = \frac{1}{2}P^2 + S[A]$ with dynamical equations

$$\begin{aligned}\dot{A} &= \frac{\partial H}{\partial P} = P \\ \dot{P} &= -\frac{\partial H}{\partial A} = -\frac{\partial S[A]}{\partial A}\end{aligned}\tag{34}$$

Since the Hamiltonian expression has no explicit time dependence, the total energy $h = \sum H_{i,\mu}$ summed over contributions from all sites and links of the lattice is constant; hence under perfect evolution of the equations the system remains on the surface of constant h . A leap-frog method is then used to march to the solution, with the momentum terms in P taking a half step at the beginning and end of the trajectory, the length of which is randomised around a fixed average time scale. The algorithm¹⁰ is set out in the pseudo code 6.

Algorithm 6 Hamiltonian Dynamics Step for general Dirac operator D . Time-march the auxiliary field according to the artificially created hamiltonian system.

```

1: function GENPROPAUX( $A^0$ )
2:   Set  $P^0 \propto \mathcal{N}(0, 1)$ 
3:   Set  $r \propto \mathcal{CN}(0, 1)$ 
4:   Set  $\phi = D^\dagger r$  for effective action  $S_{eff} = \phi^\dagger (D^\dagger D)^{-1} \phi$ 
5:   Set timestep size  $\Delta t$  and average number of timesteps  $T_{av}$ .
6:   dSdA = FORCE( $A^0$ )
7:    $P^{1/2} = P^0 + \Delta t/2$  dSdA
8:   for  $t = 0, \dots, T_{max}$  do
9:      $A^{t+1} = A^t + \Delta t P^{t+1/2}$ 
10:    dSdA = FORCE( $A^{t+1}$ )
11:    Set  $y \propto \mathcal{U}(0, 1)$ 
12:    if  $y > 1/T_{av}$  then
13:       $P^{t+3/2} = P^{t+1/2} - \Delta t$  dSdA
14:    else
15:       $P^{t+3/2} = P^{t+1/2} - \Delta t/2$  dSdA
16:      goto 100
17:     $P^{T_{max}} = P^{T_{max}-1/2} + \Delta t/2$  dSdA
18:    100 continue
19:  return  $A' = A^t, P^0, P' = P^t, \phi$ 

```

Our Thirring action splits into fermionic and auxiliary field components $S[\psi, \bar{\psi}, A] = S_F[\psi, \bar{\psi}, A] + S_G[A]$. The fermionic component uses Grassmann-valued fields $\psi, \bar{\psi}$, so we must use an equivalent action with *effective* fermionic component $S[\phi, \phi^\dagger, A] = S_{eff}[\phi, \phi^\dagger, A] + S_G[A]$, such that integration $\int \mathcal{D}\phi \mathcal{D}\phi^\dagger e^{-S_{eff}}$ over

the complex-valued ϕ, ϕ^\dagger produces an identical result to the Grassmann integral $\int \mathcal{D}\psi \mathcal{D}\bar{\psi} e^{-S_F}$, facilitating the calculation of the *force* term $\frac{\partial S[A]}{\partial A}$ incorporated in the Hamiltonian time marching. In order to generate auxiliary fields for measurements with a single fermion with operator D , we have $S_{eff}[\phi, \phi^\dagger, A] = \phi^\dagger (D^\dagger D)^{-1/2} \phi$, in which the pseudofermion field ϕ is complex. This formulation¹³ specifies the rational hybrid Monte Carlo method (RHMC).

We use domain wall operators defining $D \equiv (D_{DW}^{M1}(1))^{-1} D_{DW}^{M3}(m)$ since as $L_s \rightarrow \infty$ these have the same determinant as the overlap operator D_{OL} .¹¹ After some rearrangement via the determinant, and denoting $MS \equiv D_{DW}^{M1}(1)$ and $MT \equiv D_{DW}^{M3}(m)$, we use:¹⁷

$$S_{eff}[A] = \phi^\dagger [(MS)^\dagger MS]^{1/4} [(MT)^\dagger MT]^{-1/2} [(MS)^\dagger MS]^{1/4} \phi \quad (35)$$

In this context degrees of freedom governed by MS are sometimes referred to as Pauli-Villars fields, but it is computationally much more efficient to have MS, MT act on the same pseudofermion field ϕ . In the domain wall formulation ϕ may be considered an extradimensional pseudofermion, or a set of pseudofermions. Either way in line 4 of algorithm 6, the effective action (35) implies $D \equiv ((MT)^\dagger MT)^{1/4} ((MS)^\dagger MS)^{-1/4}$. Then $\phi = ((MS)^\dagger MS)^{-1/4} ((MT)^\dagger MT)^{1/4} r$ is set at the beginning of each trajectory and remains fixed until the next trajectory. The complex random gaussian vector $r \propto \mathcal{CN}(0, 1)$ is created independently on each site of the $2 + 1 + 1d$ lattice.

As per the action, the force terms split into a fermionic component and an auxiliary component given simply by $\frac{\delta S_G}{\delta A_{x,\mu}} = 2\beta A_{x,\mu}$. Force terms of the fermionic component, that is the derivatives of the fermionic effective action, are given by

$$\frac{\delta S_{eff}}{\delta A_{x,\mu}} = 2\text{Re} \left[\phi^\dagger \frac{\delta((MS)^\dagger MS)^{1/4}}{\delta A_{x,\mu}} \bar{\phi} \right] + \hat{\phi}^\dagger \frac{\delta((MT)^\dagger MT)^{-1/2}}{\delta A_{x,\mu}} \hat{\phi} \quad (36)$$

$$\hat{\phi} = ((MS)^\dagger MS)^{1/4} \phi \quad (37)$$

$$\bar{\phi} = ((MT)^\dagger MT)^{-1/2} \hat{\phi} \quad (38)$$

Noting for any matrix $\frac{\partial}{\partial x} M^{-1} = -M^{-1} \frac{\partial M}{\partial x} M^{-1}$, and using a partial fraction expansion of the power terms, we get

$$\begin{aligned} \frac{\delta S_{eff}}{\delta A_{x,\mu}} = & -2\text{Re} \left[\phi^\dagger \left[\sum_i \alpha_{i,1/4} ((MS)^\dagger MS + \beta_{i,1/4})^{-1} \frac{\delta((MS)^\dagger MS)}{\delta A_{x,\mu}} ((MS)^\dagger MS + \beta_{i,1/4})^{-1} \right] \bar{\phi} \right] \\ & - \hat{\phi}^\dagger \left[\sum_i \alpha_{i,-1/2} ((MT)^\dagger MT + \beta_{i,-1/2})^{-1} \frac{\delta((MT)^\dagger MT)}{\delta A_{x,\mu}} ((MT)^\dagger MT + \beta_{i,-1/2})^{-1} \right] \hat{\phi} \end{aligned} \quad (39)$$

Since $\frac{\delta((MS)^\dagger MS)}{\delta A_{x,\mu}} = (MS)^\dagger \frac{\delta MS}{\delta A_{x,\mu}} + \frac{\delta(MS)^\dagger}{\delta A_{x,\mu}} MS \neq 2\text{Re}[(MS)^\dagger \frac{\delta MS}{\delta A_{x,\mu}}]$ ^d, we have the force array $F = \frac{\partial S}{\partial A}$ given in algorithm 7.

^d $M + M^\dagger = 2\text{Re}[M]$ if M is hermitian. MS and MT are not hermitian, but all $M^\dagger M$ are hermitian.

Algorithm 7 FermRHMCForce. $\text{RATIONAL}(M, \phi, p)$ is a function returning $(M^\dagger M)^p \phi$. $\text{IMdagMPC}(M, c, \phi)$ is a function returning $(M^\dagger M + c)^{-1} \phi$.

```

1: function RHMCFORCE( $\phi$ ) % follows eqn. 39 with terms  $\frac{\delta MS^\dagger MS}{\delta A_{x,\mu}}$  expanded.
2:    $F = 0$ 
3:    $\hat{\phi} = \text{RATIONAL}(MS, \phi, pow = 1/4)$  % eqn. 37
4:    $\bar{\phi} = \text{RATIONAL}(MT, \hat{\phi}, pow = -1/2)$  % eqn. 38
5:   for all  $i \in \beta_{i,1/4}$  do % First line of eqn. 39
6:     % calc sl,sr,vl,vr
7:      $s_l = \text{IMDAGMPC}(MS, \beta_{i,1/4}, \phi)$ 
8:      $s_r = \text{IMDAGMPC}(MS, \beta_{i,1/4}, \bar{\phi})$ 
9:      $v_l = MSs_l$ 
10:     $v_r = MSs_r$ 
11:     $v_1 = \text{DOMWALLDERIVS}(s_l^\dagger, v_r, \text{STANDARD}, \text{DAG} = \text{TRUE})$ 
12:     $v_2 = \text{DOMWALLDERIVS}(v_l^\dagger, s_r, \text{STANDARD}, \text{DAG} = \text{FALSE})$ 
13:     $F = F - 2\alpha_{i,1/4} \text{Re}[v_1 + v_2]$ 
14:  for all  $i \in \beta_{i,-1/2}$  do % Second line of eqn. 39
15:    % calc t,w
16:     $t = \text{IMDAGMPC}(MT, \beta_{i,-1/2}, \hat{\phi})$ 
17:     $w = MTt$ 
18:     $v_1 = \text{DOMWALLDERIVS}(t^\dagger, w, \text{TWISTED}, \text{DAG} = \text{TRUE})$ 
19:     $v_2 = \text{DOMWALLDERIVS}(w^\dagger, t, \text{TWISTED}, \text{DAG} = \text{FALSE})$ 
20:     $F = F - \alpha_{i,-1/2}(v_1 + v_2)$ 
21:  % Apply anti-periodic bcs in time dimension
22:  for all  $x, y$  do
23:     $F(x, y, T) = -F(x, y, 1)$ 
24:  return  $F$ 

```

Also note $\frac{\delta MS}{\delta A_{x,\mu}} \equiv \frac{\delta MT}{\delta A_{x,\mu}}$ when the Shamir kernel is used, but not when the Wilson kernel is used. Pedagogical implementations of the methods used in this paper can be found online.³⁰

4.2. Monte Carlo Acceptance

The proposed auxiliary field A' is accepted as the next field in the sequence with probability $a = \min\{1, \exp(h^{prev} - h')\}$ where the total energy (Hamiltonian), h , is given by

$$h = h_g + h_f + h_p \quad (40)$$

$$h_g = \sum_{x,\mu} \frac{\beta}{2} A_{x,\mu}^2 ; h_f = S_{eff}[\phi, \phi^\dagger, A] ; h_p = \sum_{x,\mu} \frac{1}{2} P_{x,\mu}^2$$

Pseudocode is given in algorithm 8.

Algorithm 8 Monte Carlo Acceptance

```

1: function MCACCEPT( $A^{prev}, A', P^{prev}, P'$ )
2:    $h^{prev} = \text{HAMILTONIAN}(A^{prev}, P^{prev})$ 
3:    $h' = \text{HAMILTONIAN}(A', P')$ 
4:    $r$  is  $U(0,1)$ 
5:    $a = \min\{1, \exp(-h^{prev} + h')\}$ 
6:   if  $r < a$  then
7:     return  $A'$ 
8:   else
9:     return  $A^{prev}$ 

```

4.3. Relation between Overlap and Domain Wall Dirac Operators

Early in the development of the overlap operator it was noted⁹ that the domain wall operator²⁰ could be developed from the overlap formalism. There is an operator, K_{DW} , which also has an extra dimension and can be defined via the domain wall operators, for which $(K_{DW}\Psi)(1) = D_{OL}\psi$ identically when $\Psi = \{\psi, 0, \dots, 0\}$ is a vector of slices in the extra dimension. We may also calculate the inverse of the overlap operator indirectly with $D_{OL}^{-1}\psi = (K_{DW}^{-1}\Psi)(1)$. For the Wilson kernel with twisted mass it is expressed^{11,12}

$$K_{DW} = C^\dagger (D_{DW}^1(1))^{-1} D_{DW}^3(m) C \quad (41)$$

in which the ‘‘compacting’’ operators C and C^\dagger are given by

$$(C\Psi)(j) = \begin{cases} P_- \psi_j + P_+ \psi_{j+1} & 1 \leq j < L_s \\ P_- \psi_j + P_+ \psi_{j+1-L_s} & j = L_s \end{cases} \quad (42)$$

$$(C^\dagger\Psi)(j) = (C^{-1}\psi)_j \begin{cases} P_- \psi_j + P_+ \psi_{j-1+L_s} & 1 \\ P_- \psi_j + P_+ \psi_{j-1} & 1 < j \leq L_s \end{cases}$$

It is important to note that for the Pauli-Villars terms, $(D_{DW}^1(1))^{-1}$ in (41), the twisted mass formulation is *not* used.

5. Results

Following algorithm 5 to generate sequences of auxiliary fields, and algorithm 1 to measure instances of the condensate we find the following results on a $12^2 \times 12$ lattice, and look at some further properties of the algorithms.

5.1. Acceptance Rates of the Monte Carlo Step

The RHMC method takes an extant auxiliary field, and then finds a proposed auxiliary field by marching it forward using a fictitious hamiltonian dynamics step, moving it through its phase space. The proposed field is then accepted or not accepted in the Monte Carlo step. We look at the acceptance rates of this Monte

Carlo step in fig. 1, varying the non-dimensional coupling strength β . The average trajectory length is 0.5 with a time step $\Delta t = 0.05$ for both the Wilson and Shamir cases.

It is clear that under these conditions the Wilson formulation has a lower acceptance rate. In the weaker coupling range, the acceptance rate is between 0.9 and 0.95 for the Wilson formulation and between 0.95 and 1 for the Shamir formulation, and dropping to 0.65 to 0.75 and 0.8 to 0.95 respectively at the stronger coupling end of the plots.

It is notable that the acceptance rate decreases with extra-dimensional extent L_s since it is to be expected that the acceptance rate stops decreasing after achieving sufficiently large L_s .^e We will see below that using the Wilson kernel seems to have lower L_s requirements than the Shamir kernel in the critical region, supporting with the hypothesis that for fixed L_s the Wilson scheme is closer to the correct U(2)-invariant dynamics.

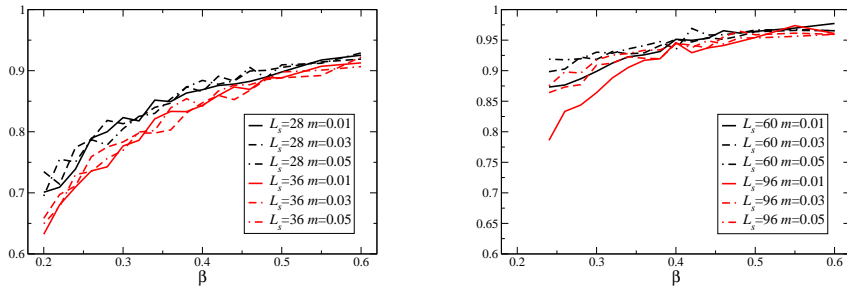


Fig. 1. Acceptance Rate in the Monte Carlo Step. L_s is the extent of the extra dimension in the domain wall formulation, and spacetime lattice is 12^3 . Note the critical region is estimated to be 0.33-0.34. Left panel: Wilson kernel. Right panel: Shamir kernel.

5.2. Eigenvalue Extrema and Condition Number of Kernel

It is useful to look at the eigenvalue range of the kernels. Since the auxiliary fields are generated dynamically, they are technically dependent on the L_s extent of the domain wall. When viewed from the overlap perspective this is not considered an extra physical dimension, but merely an expression of the level of accuracy of approximation. The left panel of Figure 2 shows the maximum and minimum eigenvalues for the Shamir kernel, and we see that the average values are largely independent of either the mass m or of L_s . At least 100 configurations were used for each data point. Auxiliary fields for the evaluation of the Shamir kernel were generated with the Shamir kernel domain wall operator, and the fields for the evaluation of the

^eThere appears to be no L_s volumetric effect on the hamiltonian dynamics step, $\dot{P} = -\frac{\partial S[A]}{\partial A}$; that is the effective action has little if any L_s -dependence for large enough L_s , and does not lead to a destabilisingly large effective time step.

Wilson kernel were generated using the Wilson kernel domain wall operator. Unlike formulations using compact link fields, the eigenvalues are not bounded from above and, for the Shamir kernel, there is a significant increase in the maximum eigenvalue beyond the critical $\beta_c \approx 0.33$.¹⁵

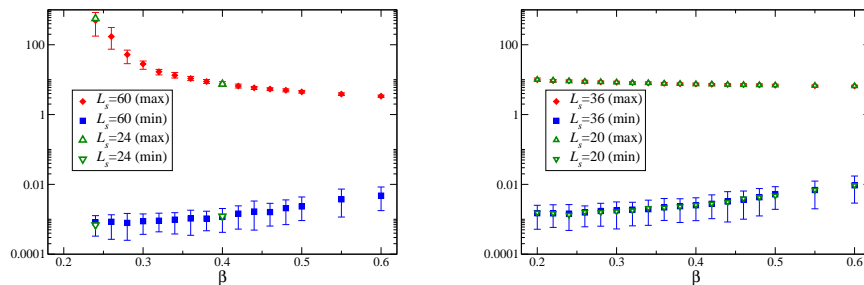


Fig. 2. Min/max kernel eigenvalues obtained with $m = 0.01$. Left panel: Shamir kernel. Right panel: Wilson kernel. Error bars show the first and ninth deciles of the eigenvalue data across the ensemble.

Plots for the Wilson kernel are shown in the right panel of Figure 2. These eigenvalues provide a guide for choosing the Zolotarev range to be used in the overlap operator, unless the range is to be reset for every auxiliary configuration. Since the latter is costly, especially for the dynamic step, it is generally preferable to choose a fixed range. Although the eigenvalues are strictly only bounded below by zero, a practical range can be identified from the plots. We have found failing to adhere strictly to the upper bound causes a larger changes in the value of $\langle \bar{\psi}\psi \rangle$ than varying the lower bound, which can be ascribed to a finite operator renormalisation on variation of the UV cutoff.

The L_s -independence, at least for all L_s above an unexplored lower bound, combined with an a priori belief that the condensate measurements require significantly higher L_s values, suggests the possibility of using different L_s values for the sea-fermions (the Dirac operator used in the generation of the auxiliary fields) and the valence fermions (the Dirac operator used for the condensate measurements).

Figure 3 indicates the effect of mesh size V on the eigenvalues, this time with *quenched* auxiliary fields (ie. generated using solely the gaussian measure $S = S_G[A]$ of eqn. (3) rather than $S = S_F[\psi, \bar{\psi}, A] + S_G[A]$). The maximum eigenvalue is V -independent for the Wilson kernel. Noting that the critical region in this case is in the vicinity of $\beta_c \approx 0.7$, we find for the Shamir kernel, the maximum eigenvalue is largely V -independent only on the symmetry unbroken side. The smallest eigenvalues for both kernels are strongly dependent on V as β moves into the strongly coupled region. The lower values reach a minimum somewhere around the critical region and then increase again. Similarly for the strongly coupled side for Shamir kernel, the maximum eigenvalue decreases again. However, the upper bound for the

Wilson kernel is monotonic. Whether the trends in these volume effects continue arbitrarily is unclear from this data, although if continued it would suggest an unbounded maximum eigenvalue for the Shamir case around the critical region. Figure 4 shows the condition numbers. In the weakly coupled limit the Shamir kernel has the lower condition number, and hence better numerical properties, whereas moving towards the stronger coupling and through the critical point the Wilson kernel has a much smaller condition number, although the value declines again for the Shamir kernel.

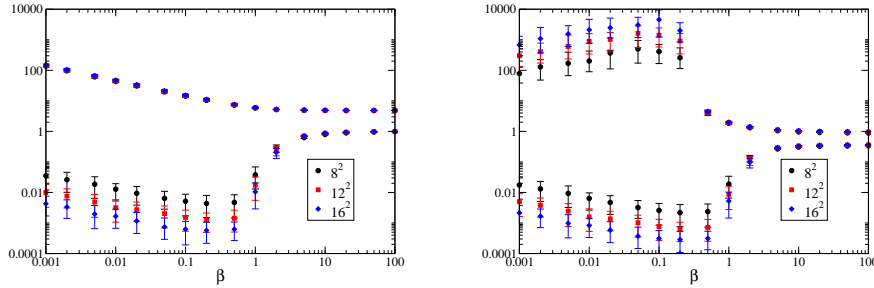


Fig. 3. Minimum and maximum kernel eigenvalues for quenched auxiliary fields on different lattice sizes (eg. 8^2 in the key refers to lattice with $N_s = 8$, $N_t = 8$). Error bars show the first and ninth deciles. Left panel: Wilson kernel. Right panel: Shamir kernel.

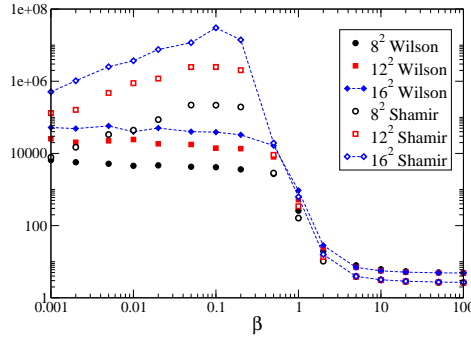


Fig. 4. Condition number of the Shamir and Wilson kernel with quenched auxiliary fields and varying lattice size.

5.3. Shamir Condensates

Next we examine condensates evaluated with the Shamir kernel, similarly to¹ but using a smaller $12^2 \times 12$ mesh size rather than the $16^2 \times 16$ meshes in those works. This is computationally beneficial not only from the decreased mesh size, but also the expected decrease in eigenvalue range of the kernel, which was noted in quenched

simulations. Although diminished, the L_s -limit challenges remain, and indeed the condensates plotted as a function of mass m in the left panel of fig. 5 for $L_s = 24, 60, 96$ do not suggest convergence in the strongly coupled region, even for $m = 0.05$.

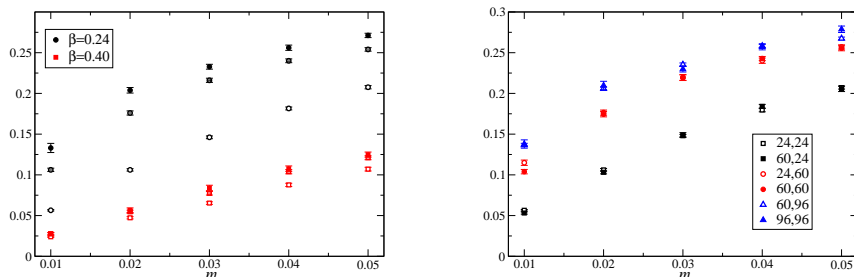


Fig. 5. Left: Dynamic condensate plots with the Shamir kernel for $\beta = 0.24, 0.40$ and $L_s = 24$ (open symbols), 60 (shaded) and 96 (filled). Right: Partially quenched Shamir condensates for $\beta = 0.24$. X,Y in the legend denotes the auxiliary fields were generated with $L_s = X$, and the measurements were taken with $L_s = Y$. At least 500 auxiliary field configurations were used in each measurement.

Following the observation that there may be no requirement for the auxiliary field to be generated with such a stringent L_s value, we look at partially quenched condensates in the right panel of fig. 5, with a strong coupling $\beta = 0.24$. As before, curves with sea and valence fermions calculated with the same L_s values are plotted, but now curves where the valence fermions, and hence the condensates, are measured with a different L_s value, are also added. The results support the intuition that the condensate measurements are controlled by the L_s of the valence fermions, and using lower L_s values for the sea fermions has a limited impact on the results. Given the high costs of dynamically generating the auxiliary fields, this represents a significant potential in computational cost cutting. Of course, there is a certain inevitability that utilising different but sufficiently large L_s values for valence and sea fermions gives the same measurement results, given the nature of L_s convergence; for high enough values of L_s the limits of machine precision will eventually be reached. Given that measurements will only ever be wanted to a certain accuracy, lower than machine precision, it seems quite reasonable that different stages of the computational process may be performed with differing levels of accuracy (which is what varying L_s represents) and still achieve the final required accuracy.

The perspective of L_s being a parameter of accuracy in the domain wall formulation only makes sense when it is formally related to the overlap operator. So-called non-bulk formulations in which the auxiliary (link) fields U applied in the Wilson operator $D_W[U]$ differ on each slice of the domain wall extra dimension, in general have no formal relation to the overlap operator, and hence there is no accuracy in a sign function to be considered.

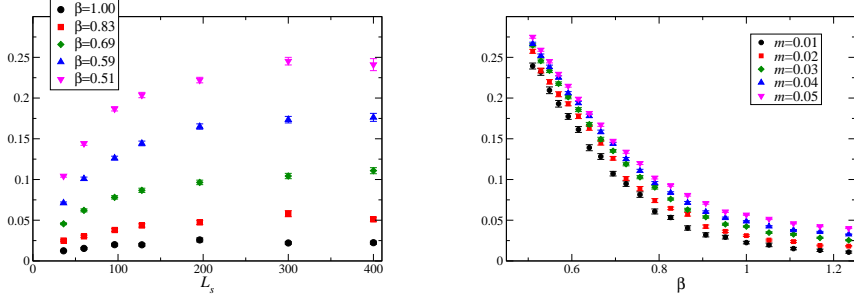


Fig. 6. Quenched calculation of condensates using Shamir kernel. Left panel: vs L_s for different coupling strengths β at $m = 0.01$. Right panel: vs β for different masses m at $L_s=300$.

We choose $L_s = 300$ for the valence fermions in further *partially quenched* condensate measurements, justified to a certain extent by the apparent convergence in quenched cases shown in fig. 6. We use the auxiliary fields dynamically generated with $L_s = 96$. The left panel of fig. 7 shows the results for $\langle \bar{\psi}\psi \rangle$ alongside those measured with $L_s = 96$. They show that the convergence has not set in by $L_s = 96$ even at relatively weak coupling. By contrast, supposing that the $L_s = 300$ is sufficient for capturing U(2)-invariant dynamics, then the right hand panel demonstrates that the sea fermions were adequately modelled, and that $L_s = 60$ or even lower would have been sufficient for the sea fermions. Condensate instances were calculated every 10 trajectories of the hamiltonian step, with at least 2000 trajectories taken.

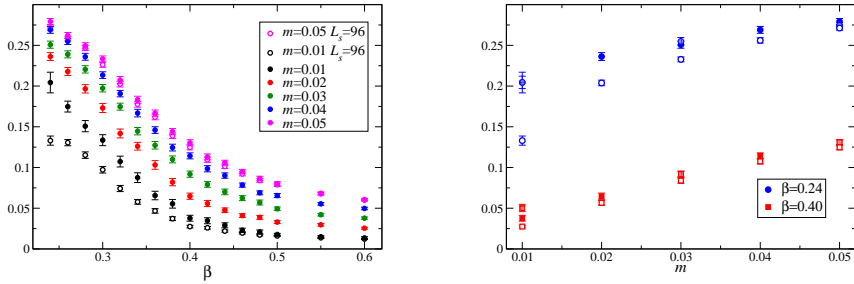


Fig. 7. Left panel: Partially quenched Shamir condensates plotted vs β using auxiliary fields generated with $L_s = 96$. Measurements were taken with $L_s = 300$ (filled) and $L_s = 96$ (open). Right panel: Partially quenched Shamir condensates measured with $L_s = Y$ plotted vs m . At least 50 configurations were used, generated with $L_s = X$, with $(X,Y)=(96,300)$ (filled), $(60,300)$ (shaded) and $(96,96)$ (open).

5.4. Wilson Condensates

Figure 8 shows condensates generated with the Wilson kernel, with instances taken every 5 trajectories over at least 1500 trajectories, using the hyperbolic tangent (HT) approximation formulation with various L_s . Eyeballing the results suggests

that the $m = 0.05$ case seems to be well L_s -converged already at $L_s = 20$, and it appears that it may be close to satisfactory convergence for $L_s = 28, 36$ for $m = 0.01$ and $m = 0.03$.

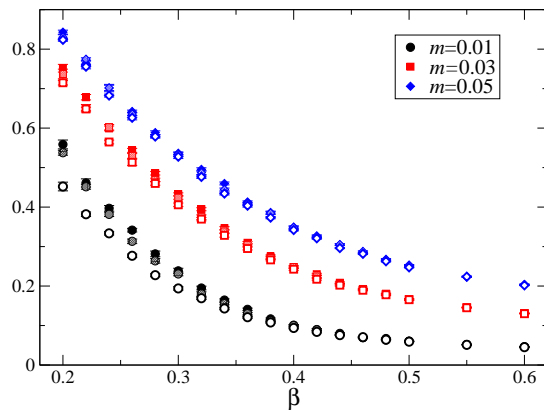


Fig. 8. Dynamic Condensate with Wilson kernel for various m , using HT formulation with $L_s = 36$ (fled), 28 (shaded), 20 (open).

This is misleading, however. The left panel of Figure 9 shows measurements using the Zolotarev formulation for the valence fermions with $L_s = 24$ and a range $[0.001, 10]$, against two different mass plots of the HT formulation. While we again see that at $m = 0.05$ the condensate appears L_s -converged, we also see that the HT formulation is not yet converged for $m = 0.01$. We argue that similarly to the Shamir case, we do not require the L_s -convergence in the generation of the auxiliary field to match that in the measurements, and hence proceed using HT-generated auxiliary fields. We also want to check that the Zolotarev range and L_s value is sufficient. The right panel of Figure 9 shows the condensates measured (still using the $L_s = 36$ generated auxiliary fields) with Zolotarev range $[0.001, 20]$ for $L_s = 18$ and $L_s = 24$, expanded to $[0.0005, 20]$ for $L_s = 30$. Based on the errors of the scalar sign function approximation we might have expected more stringent conditions to be necessary, but it appears that reasonable L_s -convergence is already achieved by $L_s = 18$.

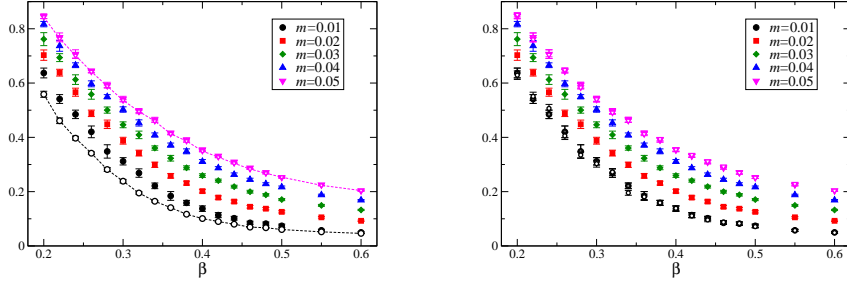


Fig. 9. Dynamic Condensate with Wilson kernel. The auxiliary fields were dynamically generated with HT and $L_s = 36$. Left panel: Measurements with Zolotarev ($L_s = 24$, Range=[0.001, 20] (filled symbols)) and HT ($L_s = 36$, open) formulations at different m . Right panel: Measurements with Zolotarev (Range=[0.001, 20]: $L_s = 18$ (open), 24 (shaded); Range=[0.0005, 20]: $L_s = 30$ (filled))

5.5. Equation of State

Finally we want to calculate an equation of state⁵ from the condensate measurements, given by eqn. (8), and estimate the critical exponents. For Dirac operators which have the same physical content, we would expect the fitted exponents to be the same: this is a manifestation of the universality expected at a critical point regardless of the microscopic details of the regularisation procedure employed. Hence the choice of Wilson or Shamir kernel should yield the same critical exponents. Fig. 10 shows two such fits with the corresponding exponents set out in table 2. As has been noted before,¹ the values are sensitive to the data set chosen to be fitted. Nevertheless we find that the results are in plausible agreement.

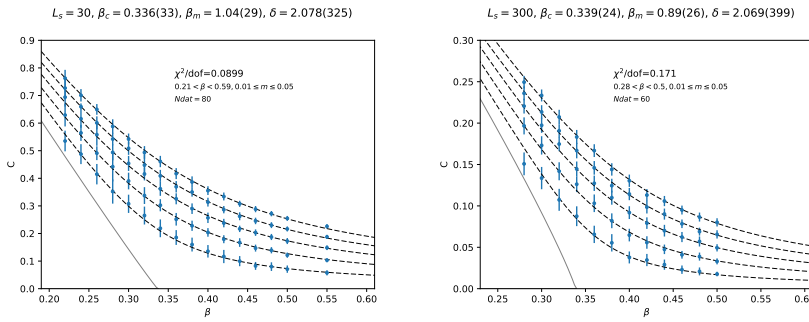


Fig. 10. Equation of State fits. Left panel: Wilson formulation. Auxiliary fields generated with HT and $L_s = 36$, measurements with Zolotarev and $L_s = 30$. Right panel: Shamir formulation. Auxiliary fields generated with HT and $L_s = 96$, measurements with Zolotarev and $L_s = 300$.

The critical exponents are consistent between the Shamir and Wilson formulations, although for β_m this within fairly large error margins. Of course, this data only hints at the similarity of the results, and more and better data is required. How-

Table 2. Equation of state critical exponents found with partially quenched Shamir HT kernel for different β data range windows. Mass range is [0.01, 0.05].

	β	β_c	β_m	δ	η	ν
Wilson	0.22-0.55	0.336(33)	1.04(29)	2.078(325)	0.95(15)	1.1(3)
Shamir	0.28-0.50	0.339(24)	0.89(26)	2.069(399)	0.96(18)	0.91(28)

ever, significant differences are found from the values given in.^{17,24} The exponents found with a Shamir kernel on $16^2 \times 16$ mesh were $\beta_c = 0.320(5)$, $\beta_m = 0.320(5)$, $\delta = 4.17(5)$, corresponding to $\nu = 0.55(1)$ and $\eta = 0.16(1)$. We attribute the difference to the lack of L_s -convergence in earlier work. Further comparison with a staggered formulation may be considered which gave⁵ $\beta_m = 0.57(2)$, $\delta = 2.75(9)$, corresponding to $\nu = 0.60(4)$ and $\eta = 0.71(3)$. Differences here are thought to stem from formulational differences.

6. Summary

We have made progress in overcoming the challenging L_s limit of the overlap operator in the context of the planar Thirring model at a critical point, yielding distinct results from similar earlier enterprises, albeit on a relatively small mesh size.

A number of different aspects of the Dirac operators and their implementations were investigated. Eigenvalue ranges of the overlap kernel were explored, and a key finding is that the non-compact link fields leads to kernel eigenvalues apparently unbounded from above, whereas these are clearly bounded with compact link fields. This has very significant (detrimental) implications on the computational difficulty of inverting the Dirac operator. Further, the Shamir formulation appears to become more challenging as the mesh gets larger in a way that the Wilson kernel doesn't. That is, that the largest kernel eigenvalue increases with mesh size around and beyond the critical coupling strength.

A key finding, or observation, to carry to future work, was that the level of accuracy corresponding to the large L_s limit required in the measurement of the condensate, is not required in the generation of the auxiliary fields. Given that the bulk of computational effort in dynamic simulations is in the generation of the auxiliary fields this has the potential to save significant computational cost. Further, rather than being a tradeoff with the Monte Carlo acceptance rate, L_s reduction improves the acceptance rate.

The (expected) superiority of the Zolotarev approximation was demonstrated to be necessary to achieve L_s -convergence of the measurements with a modest value of L_s , although a modest L_s value with the HT approximation appeared to be sufficient for the auxiliary field generation.

We calculated an equation of state and critical exponents for both Wilson and Shamir kernels, using low accuracy for the generation of the auxiliary fields and high accuracy for the measurements. Although better statistics would be desirable, the results are consistent between the formulations, as we would hope. This was

particularly good news as lower L_s -range preliminary work had hinted that consistency may not have been found. This would not have been possible without partial quenching.

Acknowledgments

This work used the DiRAC Data Intensive service (CSD3) at the University of Cambridge, managed by the University of Cambridge University Information Services on behalf of the STFC DiRAC HPC Facility (www.dirac.ac.uk). The DiRAC component of CSD3 at Cambridge was funded by BEIS, UKRI and STFC capital funding and STFC operations grants. DiRAC is part of the UKRI Digital Research Infrastructure. Further work was performed on the Sunbird facility of Supercomputing Wales. The work of JW was supported by an EPSRC studentship, and of SH by STFC Consolidated Grant ST/ST000813/1.

References

1. S. Hands, Phys. Rev. D **99** (2019) no.3, 034504 doi:10.1103/PhysRevD.99.034504 [arXiv:1811.04818 [hep-lat]].
2. W.E. Thirring, Annals Phys. **3** (1958), 91-112 doi:10.1016/0003-4916(58)90015-0
3. S. Hands, JHEP **09** (2015), 047 doi:10.1007/JHEP09(2015)047 [arXiv:1507.07717 [hep-lat]].
4. P.H. Ginsparg and K.G. Wilson, Phys. Rev. D **25** (1982), 2649 doi:10.1103/PhysRevD.25.2649
5. L. Del Debbio *et al.* [UKQCD], Nucl. Phys. B **502** (1997), 269-308 doi:10.1016/S0550-3213(97)00435-5 [arXiv:hep-lat/9701016 [hep-lat]].
6. S. Christofi, S. Hands and C. Strouthos, Phys. Rev. D **75** (2007), 101701 doi:10.1103/PhysRevD.75.101701 [arXiv:hep-lat/0701016 [hep-lat]].
7. B.H. Wellegehausen, D. Schmidt and A. Wipf, Phys. Rev. D **96** (2017) no.9, 094504 doi:10.1103/PhysRevD.96.094504 [arXiv:1708.01160 [hep-lat]].
8. H. Neuberger, Phys. Lett. B **417** (1998), 141-144 doi:10.1016/S0370-2693(97)01368-3 [arXiv:hep-lat/9707022 [hep-lat]].
9. R. Narayanan and H. Neuberger, Nucl. Phys. B **443** (1995), 305-385 doi:10.1016/0550-3213(95)00111-5 [arXiv:hep-th/9411108 [hep-th]].
10. A.D. Kennedy, in *Perspectives in Lattice QCD* (ILFTN workshop, World Scientific) [arXiv:hep-lat/0607038 [hep-lat]]
11. S. Hands, Phys. Lett. B **754** (2016), 264-269 doi:10.1016/j.physletb.2016.01.037 [arXiv:1512.05885 [hep-lat]].
12. R. C. Brower, H. Neff and K. Orginos, Comput. Phys. Commun. **220** (2017), 1-19 doi:10.1016/j.cpc.2017.01.024 [arXiv:1206.5214 [hep-lat]].
13. A.D. Kennedy, I. Horvath and S. Sint, Nucl. Phys. B Proc. Suppl. **73** (1999), 834-836 doi:10.1016/S0920-5632(99)85217-7 [arXiv:hep-lat/9809092 [hep-lat]].
14. M.A. Clark, PoS **LAT2006** (2006), 004 doi:10.22323/1.032.0004 [arXiv:hep-lat/0610048 [hep-lat]].
15. J.A.G. Worthy, PhD Thesis, Swansea University, Swansea (2024).
16. S. Hands and B. Lucini, Phys. Lett. B **461** (1999), 263-269 doi:10.1016/S0370-2693(99)00843-6 [arXiv:hep-lat/9906008 [hep-lat]].
17. S. Hands, M. Mesiti and J. Worthy, Phys. Rev. D **102** (2020) no.9, 094502 doi:10.1103/PhysRevD.102.094502 [arXiv:2009.02964 [hep-lat]].

18. B. Jegerlehner, [arXiv:hep-lat/9612014 [hep-lat]].
19. A. Borici, Nucl. Phys. B Proc. Suppl. **83** (2000), 771-773 doi:10.1016/S0920-5632(00)91802-4 [arXiv:hep-lat/9909057 [hep-lat]].
20. D.B. Kaplan, Phys. Lett. B **288** (1992), 342-347 doi:10.1016/0370-2693(92)91112-M [arXiv:hep-lat/9206013 [hep-lat]].
21. C. Gattringer and C. B. Lang, Lect. Notes Phys. **788** (2010), 1-343 Springer, 2010, ISBN 978-3-642-01849-7, 978-3-642-01850-3 doi:10.1007/978-3-642-01850-3
22. M.A. Clark, A.D. Kennedy, <https://github.com/mikeaclark/AlgRemez>, 2005.
23. Y. Shamir, Nucl. Phys. B **406** (1993), 90-106 doi:10.1016/0550-3213(93)90162-I [arXiv:hep-lat/9303005 [hep-lat]].
24. S. Hands, M. Mesiti and J. Worthy, PoS **LATTICE2021** (2022), 539 doi:10.22323/1.396.0539 [arXiv:2110.03944 [hep-lat]].
25. E.I. Zolotarev, Zap. Imp. Akad. Nauk. St. Petersburg, **30**, (1877)
26. T. W. Chiu, Phys. Rev. Lett. **90** (2003), 071601 doi:10.1103/PhysRevLett.90.071601 [arXiv:hep-lat/0209153 [hep-lat]].
27. A.D. Kennedy, Nucl. Phys. B Proc. Suppl. **128** (2004), 107-116 doi:10.1016/S0920-5632(03)02466-6 [arXiv:hep-lat/0402037 [hep-lat]].
28. A.D. Kennedy, [arXiv:hep-lat/0402038 [hep-lat]].
29. J. Worthy, <https://github.com/JWorthy77/ZCode>, 2022.
30. J. Worthy, <https://github.com/JWorthy77/TCondensate>, 2024.